Ultrasonics 98 (2019) 99–107

Contents lists available at ScienceDirect

Ultrasonics

journal homepage: www.elsevier.com/locate/ultras

Artifacts detection-based adaptive filtering to noise reduction of strain imaging

Dangguo Shao[a,*], Ye Yuan[a], Yan Xiang[a,*], Zhengtao Yu[a], Paul Liu[b,c], Dong C. Liu[b,c]

[a] Faculty of Information Engineering and Automation, KunMing University of Science and Technology, KunMing, China
[b] School of Computer Science, Sichuan University, Chengdu, China
[c] Saset Healthcare Inc. Chengdu, China

ARTICLE INFO

Keywords:
Statistical analysis
Local histogram
Adaptive filter
Ultrasonic strain imaging

ABSTRACT

Strain imaging in medical ultrasound is the imaging modality of elastic properties of biological tissue. In general, strain image will suffer from artifacts noise, which degrades lesion detectability and increases the likelihood of misdiagnosis. How to both suppress artifacts effectively and preserve the structure is vital for diagnosis and also for image post-processing. The bilateral filtering can reduce artifact noise and, at the same time, maintain the tissue structure. However, the balance between noise suppression and edge preservation often makes the threshold selection difficult. This paper is to solve the problem of difficult threshold selection in bilateral filtering. The probability distribution function of amplitude modulation noise in this paper is derived from the statistics of uncompressed speckle. The statistical model of artifact formation is useful for designing an adaptive fast bilateral filter for artifact reduction in ultrasound strain imaging. Both simulation and phantom testing show that the proposed method can improve the quality of ultrasonic strain imaging. Furthermore, the elastographic signal-to-noise ratio was increased by 129.91% and 52.36% for simulated and phantom strain images. The elastographic contrast-to-noise ratio was increased by 521.42% and 218.07% for simulated and phantom strain images, respectively. As indicated by the profiles, the proposed method produces a better result for the purpose of visualization.

1. Introduction

Strain imaging in medical ultrasound is an imaging technique that displays information about tissue stiffness [1–3]. Strain imaging has been proved to be useful in different clinical applications including the diagnosis of breast cancer and prostate [4], monitoring of high intensity focused ultrasound lesions [5], imaging the myocardium [6] and monitoring thermal changes and ablation [7]. However, Strain imaging [8,9] suffers from artifact noise which may come from two dominant sources: decorrelation error and amplitude modulation (AM) error. Decorrelation error [10–12] is caused by compression, deformation, slide-slippage, and other movement sources, which make the motion tracking not follow the conventional time delay estimation model. AM error [13] is caused by the random fluctuation of signal amplitude, which makes the location of the displacement estimate out of the center of the analysis window.

Some research groups have proposed approaches to suppress artifact noise, including amplitude compression [14], multi-compression averaging [15], signal stretching [16], wavelet denoising [17], amplitude modulation correction [18], compounding approach [19–26], bilateral filtering [27,29] and Other technologies [28,30–33]. Compounding approach includes methods in which the data acquisition procedure has been modified to produce several images of the same region, images that are partially correlated or non-correlated, and then combine them to form a single image. Decorrelation among the individual images is obtained by generating each original image while the transducer is located at different spatial locations [19–24], or while the transducer operates at different frequencies [25,26]. Wavelet denoising [17] is a post image formation filtering approach. But these methods do not utilize the information about the artifact contained in the images. The methods of amplitude compression, stretching and modulation correction (AMC) use the information about signal amplitude, which helps the location of the displacement estimate to approximate the center of the analysis window. The bilateral filtering [27,29] can reduce artifact noise and, at the same time, maintain the tissue structure. However, the balance between noise suppression and edge preservation often makes the threshold selection difficult. This paper is to solve the problem of difficult threshold selection in bilateral filtering. The

* Corresponding authors.
E-mail addresses: huntersdg@126.com (D. Shao), sharonxiang@126.com, 50691012@qq.com (Y. Xiang).

https://doi.org/10.1016/j.ultras.2019.05.007
Received 16 April 2018; Received in revised form 3 April 2019; Accepted 22 May 2019
Available online 23 May 2019
0041-624X/ © 2019 Published by Elsevier B.V.

Probability Distribution Function (PDF) of AM noise will be derived from AM error on the basis of the statistics of uncompressed speckle in this paper. The statistical model of artifact formation is useful for designing a good adaptive filter for artifact reduction in ultrasonic strain imaging. A histogram matching technique is applied to detect artifacts noise. The artifacts detection derive an adaptive similarity value to adjust smoothing. Evaluation methods are demonstrated in both simulation and phantom testing.

The organization of the paper is as follows. Section 2 derives the statistical model of amplitude modulation noise in ultrasonic strain imaging. Detection and application of amplitude modulation noise are given in Section 3. Simulations and experiment are manifested in Section 4, including the usage of quantitative quality metrics and the results. And discussion and conclusion are presented in Section 5 and 6, respectively.

2. Theory

A strain image can be produced by displaying spatial derivatives from the displacement field which is from the estimate of the time shift. But in fact, the estimate of the time shift between two signals obtained before and after target compression is affected by the signal amplitude. If the strain estimates are obtained directly from the time shift measurement, this effect results in an undesired random modulation of the strain estimates by the random signal envelope amplitude. Hence, a displacement estimate doesn't often closely track displacement at the window center. The actual location is skewed towards higher amplitude portions of the windowed signal [14]. The distribution of signal envelope amplitudes follows some statistical distribution (e.g., Rayleigh if there is a large number of small randomly distributed scatterers [16]), and the added variability due to the strain modulation effect is related to that envelope amplitude distribution. In general, the signal envelope amplitude is independent of the elasticity of the medium; the elastographic noise introduced by the undesirable leakage of signal envelope amplitude information into the strain estimations is considered an artifact [16].

Coherent summation of received echoes from sub-resolvable scatterers creates constructive and destructive interference that appears as speckle for signal magnitude and also similarly causes fluctuations in phase [13]. One consequence is that correlations become skewed toward the larger-power portion of signal by constructive interference. Lindop et al. [18] noted that traditional window matching approaches can be enhanced. The actual estimation location can be treated as a random variable, with low probability density at window ends and higher probability at the center. For the sake of clarity, we analyze the simplest estimate of 1-D strain, e, where 1-D displacement estimates are differenced and divided by the spacing between them:

$$e = \frac{\Delta d}{\Delta l} = \frac{d_2 - d_1}{l_2 - l_1} \tag{1}$$

where d_1 and d_2 are displacement estimates from windows 1 and 2 respectively, and l_1 and l_2 record the estimation locations, which are not in general the same as the centers of the windows. It is sometimes assumed that Eq. (1) contains only two random variables, d_1 and d_2. In [18], Lindop et al. examines the other variables, l_1 and l_2. The two sources of estimation noise are illustrated in Fig. 1.

Lindop [18] refer to the location estimation technique as amplitude modulation correction.

(AMC). Its application is illustrated in Fig. 2. In AMC, a location estimate, l_m, is produced by substituting these expressions into Eq. (2).

$$l_m = \frac{\sum_{t=m\Delta t}^{m\Delta t+n} W(t, d_m)t}{\sum_{t=m\Delta t}^{m\Delta t+n} W(t, d_m)} \tag{2}$$

where n is the correlation window size at axial. The location estimate, l_m, is defined to be the location at which the displacement estimate

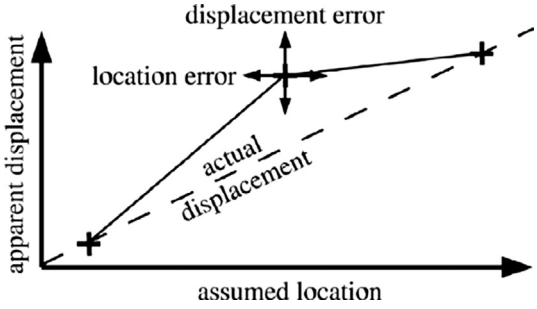

Fig. 1. A practical displacement estimate is shown between two ideal estimates, where estimation error causes it to deviate from the actual displacement in the underlying tissue. There are two noise sources, as indicated by the labelled arrows.

approximation equals the actual displacement. In other words, location estimates are produced by evaluating the centroid of a set of weighting estimates after windows have been matched for displacement estimation purposes. The combination of refined location estimates with the same displacement estimates yields greater accuracy overall in the correspondence between the estimates and the actual displacement field. It also results in more accurate correspondence between tissue features' physical locations and their apparent locations in strain images.

In Eq. (2), expression of $W(t)$ is as follows in accordance with AMC [18].

$$W(t) = X_1 \times X_2 \tag{3}$$

where X_1 and X_2 are the signal envelope amplitude of two signals obtained before and after target compression. We knew that the distribution of signal envelope amplitudes follows Rayleigh distribution [24,26] if there are a large number of small randomly distributed scatterers. The signal envelope amplitude is assumed as an independent random variable. The input-output relationship for a Rayleigh distribution is demonstrated by the following

$$p(X) = \frac{X}{\sigma_0^2} e^{-\frac{X^2}{2\sigma_0^2}}, X \geqslant 0 \tag{4}$$

where σ_0 is the parameter of Rayleigh distribution. In this paper, we have made further deductions. According to Appendix A, W(t) follows exponential distribution.

$$p(W) = \lambda e^{-\lambda W} \tag{5}$$

where λ is the parameter of exponential distribution. Further in accordance with Appendix B, the PDF of l_m is as follows.

$$p(l_m) = \frac{\lambda^{2n}}{\Gamma(n)} \sum_{i=1}^{n} \left[\frac{(\lambda_i l_m + \lambda)^{-(n+1)}}{\prod_{\substack{j=1 \\ i \neq j}}^{n} (\lambda_j - \lambda_i)} \right] \tag{6}$$

where n and λ are the parameters of the PDF.

A strain image can be produced by displaying spatial derivatives from the displacement field. Therefore, the Δl can be considered the first derivative of l_m.

$$\Delta l(m) = (l_m)' \tag{7}$$

Finally, from Appendix C, the PDF of Δl is as follows.

$$p(\Delta l) = A \sum_{i=1}^{n} \frac{i^{2n-1} \Delta l \cdot \left[\frac{(\Delta l)^2}{2} + c + i \right]^{-(n+1)}}{\prod_{\substack{j=1 \\ i \neq j}}^{n} (i - j)} \tag{8}$$

where n is the correlation window size at axial, A is amplitude of function and c is a translational variable. From our deduction, we can

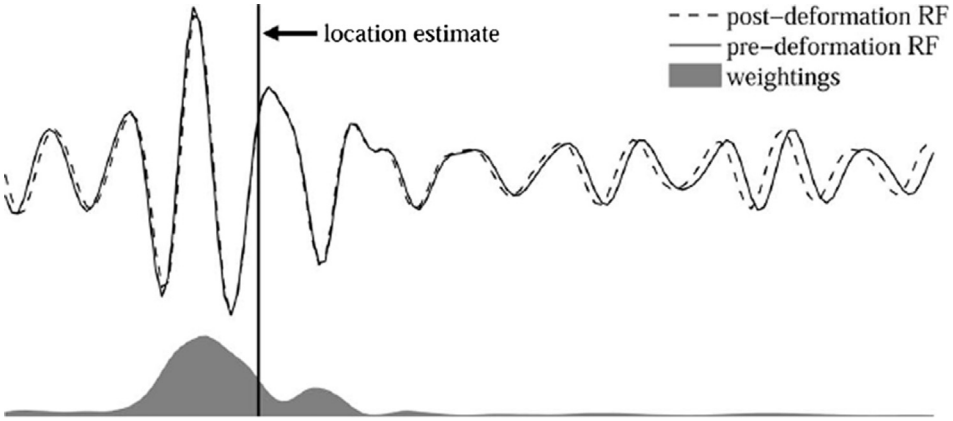

Fig. 2. Example of AMC:Phase zero estimation is employed to align pre- and post-deformation windows. AMC is applied to refine the location of the displacement estimate.

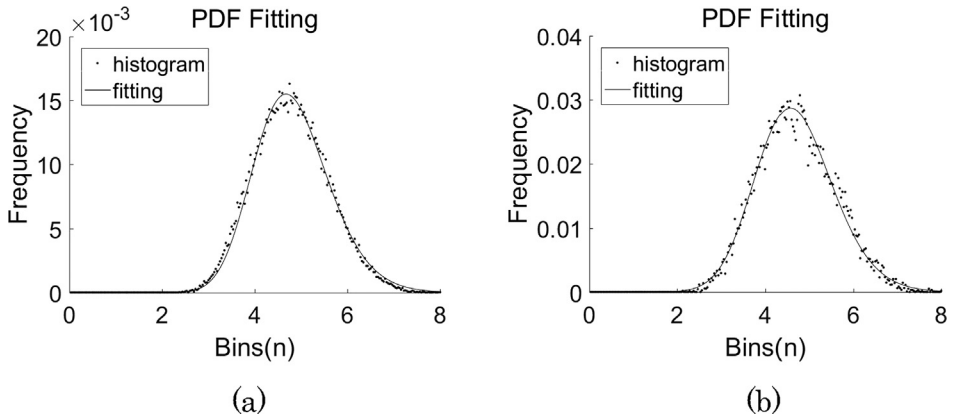

Fig. 3. (a) Histogram of simulated strain noise; (b) Histogram of phantom strain noise.

see that artifact noise obeys a certain distribution. This distribution can be represented by a histogram. We use formula (8) to fit the histogram of the artifact noise. Fig. 3 are the fitting results of the histograms in simulation and phantom strain noise respectively. Fig. 3(a) is a simulated data which the center frequency is 7.5 MHz, the correlation window size is 10 pixels and overlap is 0.85 in ultrasonic strain imaging; correspondingly, A is 1.58, n is 10 and c is 1.6. Fig. 3(b) is a phantom data which the center frequency is 5 MHz, the correlation window size is 20 pixels and overlap is 0.8 in ultrasonic strain imaging; correspondingly, A is 3.3, n is 20 and c is 3.1. We can observe that the fitting results are good in simulation and phantom respectively. In this paper, the discovery of the statistical law of artifacts lays a theoretical foundation for the detection of artifacts.

3. Methods

3.1. Histogram matching-based amplitude modulation noise detection

It is required that amplitude modulation noise detection be used for adaptive strain noise suppression algorithms. According to Section 2, the above Eq. (8) can be used to model the statistics of amplitude modulation noise in ultrasonic strain imaging. In this paper, we use the local amplitude histogram to extract the information of inherited distribution function of strain noise statistics. The histogram for a reference region has a characteristic shape, which defines it as a region dominated by strain noise. Other histograms have different shapes and are thus assumed to contain more structure in the block.

To have a reliable strain noise statistics, the size of the processing window must be chosen at the outset of the filtering procedure. And the size should be big enough to cover a region with at least one resolution cell. In [34], Alam et al. studied axial resolution criteria in Elastographic.

$$R = -0.0498 + 0.15867T + 0.8982\Delta t \tag{9}$$

where R is the resolution, T is the correlation window size, and $\triangle$t is the window shift. We display the surface plot of the fit for the range of data used in the fit ($0.5 \le T \le 4$, $0.0625 \le \triangle t \le 2$, $\triangle t \le T$; all units in millimeters). The results in [35] show that the elastographic lateral resolution is proportional to the beamwidth of the US system. An empirical expression of the elastographic lateral resolution is given by

$$Rl = 1.708 \cdot \lambda \cdot (f - number) \tag{10}$$

where λ is the wavelength and the *f-number* is the ratio of the focal length to the diameter of the transducer.

In [36,37], the optimal number of bins to represent a normal (Gaussian) distribution with a 95% confidence level is.

$$\text{Number of bins} = 1.87(nn - 1)^{2/5} \tag{11}$$

and the number of bins could be 8 for $nn = 49$, i.e., from a 7×7 local window. Eq. (11) could be used to approximately determine the number of bins of more practical distribution, such as the double exponential from the compressed images.

If the processing window contains some resolved structure, its histogram always shows a bias in shape, for example, narrow for echo-free region and wide for specular reflectivity area or even multimodal for edges. These will result in “less similar” to the reference histogram of fully developed strain noise. Also, for low-contrast objects, histograms from different objects will also be different, for example, the width of the histograms is also a function of tissue type. In this paper, the similarity value of two histogram shapes has been defined by comparing

the two histograms bin by bin through a user-controlled error function:

$$S_{ij} = 1 - \frac{1}{nnL}\sum_{k=1}^{L}\frac{H_{ij,k} - H_{r,k} + nn}{2} \tag{12.1}$$

$$\sum_{k=1}^{L} Hi_{j,k} = \sum_{k=1}^{L} H_{r,k} = nn \tag{12.2}$$

where $H_{ij,k}$ and $H_{r,k}$ denote the observed frequency and expected frequency respectively, and nn is the total number of sampling points. L is the length of histograms. The S_{ij} is from 0 to 1. A large similarity value (i.e., close to 1) means the processing histogram is very similar to the reference histogram. Otherwise, a small similarity means the histogram is very likely a tissue structure. The local region is classified by different similarity value. The classified result can be used to reduce strain noise in adaptive fast bilateral filter.

3.2. Adaptive fast bilateral filter

A conventional bilateral filter [27,38,39] is a non-linear technique that can blur an image while preserving sharp or distinct edges. This nonlinear filter takes both intensity and spatial proximity metrics into account. According to [29,40], the fast formation of the bilateral filter can be derived. The input-output relationship for the fast bilateral filter is demonstrated by the following:

$$BF[I_p] = \frac{\sum_{j\in I} H(j)B(||p-q||)G_\sigma(|I_p - jl)j}{\sum_{j\in I} H(j)B(||p-q||)G_\sigma(|I_p - jl)} \tag{13}$$

where $H(j)$ is the j-th bin of the histogram, S is the p-centric set of local pixels, and q is the element of S. Iq is the gray value of q pixel. $||p - q||$ is the Euclidean distance between the local pixel q and the center pixel p in the set. $|I_p - I_q|$ is the brightness distance between the local pixel q and the center pixel p. G_σ is a Gaussian function which σ is its standard deviation, and B is a normalized box function. Eq. (13) above is an approximate expression while the bins of histogram are fewer than gray levels in the range of intensity. The summing histograms is an O(1) operation with respect to the number of accumulated pixels. It depends only on the size of the histogram, which is itself a function of the bit depth of the image. On the other hand, the filtering process can be iterated multiple steps if the only one filtering step is not adequately smoothing for strain noise reduction. The standard deviation in the bilateral filter, σ, is determined by Eq. (14).

Variance can be considered as threshold to adjust the smoothing in bilateral filtering. In a traditional bilateral filter, variance is a fixed value, but it is relatively difficult to select the value for an ultrasound image. Therefore, a fixed value is not appropriate to reduce strain noise. In this paper, the variance is adapted using a local histogram matching approach based on ultrasonic strain noise. In histogram matching, a large similarity value (i.e., close to 1) means the processing histogram is very similar to the reference histogram. It also means that the processing region should been fully smoothed, and hence a larger variance is needed. Otherwise, a small similarity means the processing histogram is very likely a tissue structure and hence a smaller variance is needed to stop smoothing. Variance can be adjusted adaptively by the following expression in this paper.

$$\sigma_{ij}^2 = (Th \cdot S_{ij}^{\beta} + 1)^2 \tag{14}$$

where S_{ij} denotes the similarity value of two histograms at i,j location and β is exponent of similar. Th is an empirical value. Th is 50 and β is 2 in this paper. The Equation (14) ensures that the standard deviation of the bilateral filter is adaptive within a reasonable range, such as from 1 to 51. And Th and β can be adjusted according to different applications.

4. Results

4.1. Criteria for quantifying algorithm performance

Two main image quality metrics in ultrasonic strain imaging, the elastographic signal-to-noise ratio (SNRe) [24] and the elastographic contrast-to-noise ratio (CNRe) [26], are applied to both simulation and phantom images. SNRe quantifies the level of noise as the ratio of mean to standard deviation of strain values. And CNRe quantifies the level of contrast between a region of interest and the background. They are calculated as:

$$SN\mathrm{Re} = \frac{\mu}{\sigma} \tag{15}$$

$$CN\mathrm{Re} = \frac{2\cdot(\mu_t - \mu_b)^2}{\sigma_t^2 + \sigma_b^2} \tag{16}$$

where μ_t is the mean of a region of interest, and μ_b and σ_b are the mean and variance of similar sized regions in the image background. *upSNRe* and *upCNRe,* which are the growth rates of two image quality metrics, are defined as follows.

$$upSN\mathrm{Re} = 100\cdot\left(\frac{SN\mathrm{Re}_{result}}{SN\mathrm{Re}_{original}} - 1\right) \tag{17}$$

$$upCN\mathrm{Re} = 100\cdot\left(\frac{CN\mathrm{Re}_{result}}{CN\mathrm{Re}_{original}} - 1\right) \tag{18}$$

4.2. Strain simulation

In this study, Paul' simulation method [24] is used. And deformation model at axial in [41] is used. K is chosen to be 3.2 = 80 kPa/25 KPa to match our elastic phantom. P is chosen as 0.001, a reasonable actual deformation amount. We simulate a 7.5-MHz center frequency probe with 128 elements, 0.3 mm element width, and 0 kerf. Impulse response is a Hanning windowed 2-cycle sine. We use a 2-cycle sine excitation pulse. We use all 128 channels. One scatterer located at 1.5 cm is imaged. We form 100 beam lines within a 0.5 cm field of view. For displacement estimation, we use phase zero [11]. All versions of phase zero for the simulation use the same parameters: 0.12 cm, or 12 samples, window length; 0.03 cm, or 3 samples, distance between adjacent windows; iteration number of one. Strain is computed by a low-pass digital differentiator [8].

Own to assume that random variable is independent; we select smaller overlap to ensure the independence. In simulation, Fig. 4 shows the values of SNRe and CNRe in strain which overlap is from 0.0 to 0.85. The artifact reduced strain images are shown in Fig. 5(b)–(f) with better contrast resolution than the original images in Fig. 5(a) when remaining useful clinical information. And the strain images filtered by the adaptive bilateral filter are shown in Fig. 5(f) with better contrast resolution than others images in Fig. 5(b)–(d). The grow up of SNRe and CNRe values of the strain image in simulation are 129.91% and 521.42%, respectively, in the proposed method.

4.3. Phantom strain

For experimental data, we use a model elastic phantom. The phantom is based on the model 049 CIRS elastic QA phantoms (Computer Imaging Reference Systems, Inc., Norfolk, VA). A 0.5-cm-radius spherical cyst is placed 1.5 cm below the phantom surface. The CIRS phantom has a background of 25 kPa and includes an 80-kPa cyst. We use freehand deformation from the probe without any apparatus, such as a metal plate, which controls boundary conditions. Two frames are manually selected from a sequence. We use rectangular apodization with f-number of 1 to yield the largest lateral bandwidth possible. We find rectangular apodization to work better than any other apodization

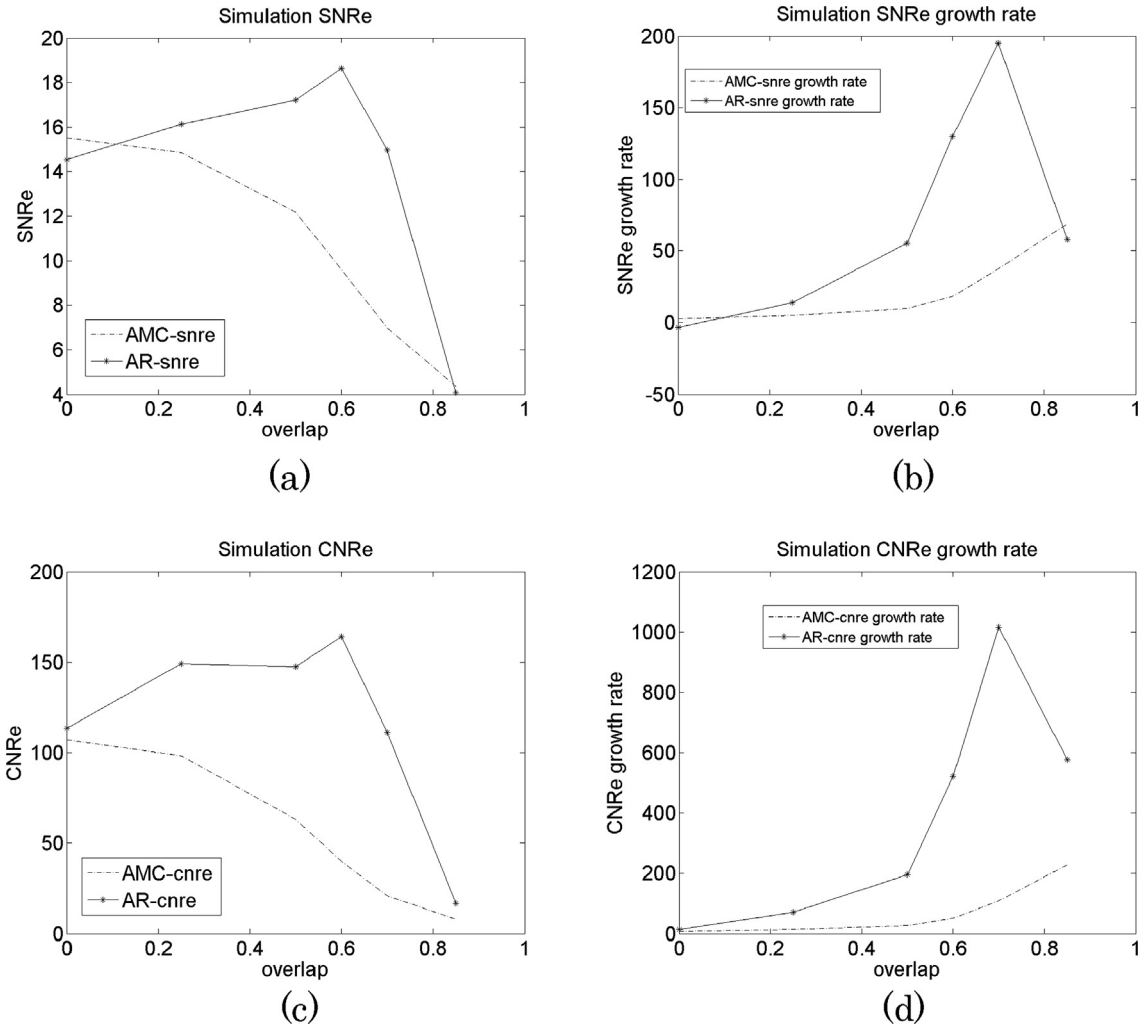

Fig. 4. Simulated strain image which overlap is from 0.0 to 0.85, the correlation window size is 8 and window size of filter is 11 × 11 pixels. (a) SNRe; (b) Grouth rate of SNRe; (c) CNRe; (d) Grouth rate of CNRe.

because we need as much energy as possible at higher lateral frequencies. Our probe has 128 elements, and our Imago C21 system has 128 channels, giving us the potential to use the entire aperture. Because our scan image has depth of 3 cm and probe is 3.8 cm wide, we may preserve our f-number choice for all depths in our scan area. We form 188 beam lines for this scan. From phantom data (Fig. 6), the same performance is obtained. In experiment of phantom, the artifact reduced strain images are shown in Fig. 6(b)–(f) with better contrast resolution than the original images in Fig. 6(a) when remaining useful clinical information. In the proposed method, the grow up of SNRe and CNRe values of the strain image in phantom are 52.36% and 218.07%, respectively. And this indicates again that the method of this paper is efficient to reduce the artifact noise and, at the same time, maintain the tissue structure.

5. Discussion

The traditional bilateral filtering method has achieved good results in ultrasonic denoising. However, the balance between noise suppression and edge preservation in bilateral filtering often makes threshold selection difficult. A small threshold, as shown in Figs. 5(c) and 6(c), produces unsatisfactory noise suppression in artifact noise areas; on the contrary, a large threshold, as shown in Figs. 5(d) and 6(d), often leads to smooth in edge regions. So in order to choose the threshold flexibly, the fixed threshold should be changed. In the proposed algorithm, the threshold, that is the standard deviation of the range filters, is adapted using a histogram matching approach based on artifacts detection. Artifact noise must be detected in order to adapt the threshold. And in order to detect artifact noise, it is necessary to identify artifact noise, that is, to find the characteristics of artifact noise. For this reason, we deduce the distribution function of artifact noise, which lays a theoretical foundation for the recognition of artifact noise. Then, we use the method based on local histogram matching to detect artifact noise. The results of artifact noise detection are expressed by similarity values, as shown in Figs. 5(e) and 6(e). As can be seen from the figures, the matching degree values of organizational edges are relatively small; correspondingly, the threshold of filtering, that is variance, is relatively small. In bilateral filters, small variance means that it is not smooth, that is, edge-preserving. This is precisely the edge preservation process needed by the organization's edge. On the contrary, the similarity value in the noise area is larger, which corresponds to the smoothing process needed in the noise area.

To examine the visual improvements, we focused on artifacts reduction and the structure preservation. The performance quality of experiments, in terms of SNRe and CNRe are applied. Quantitatively, from Fig. 4, both CNRe and SNRe from the method in this study are larger than that from AMC method. And the performances from the method in this study, as Figs. 5(f) and 6(f), are better than that of AMC method and the bilateral filtering of the fixed threshold, especially in CNRe. From the artifact reduced strain images, the method of this paper

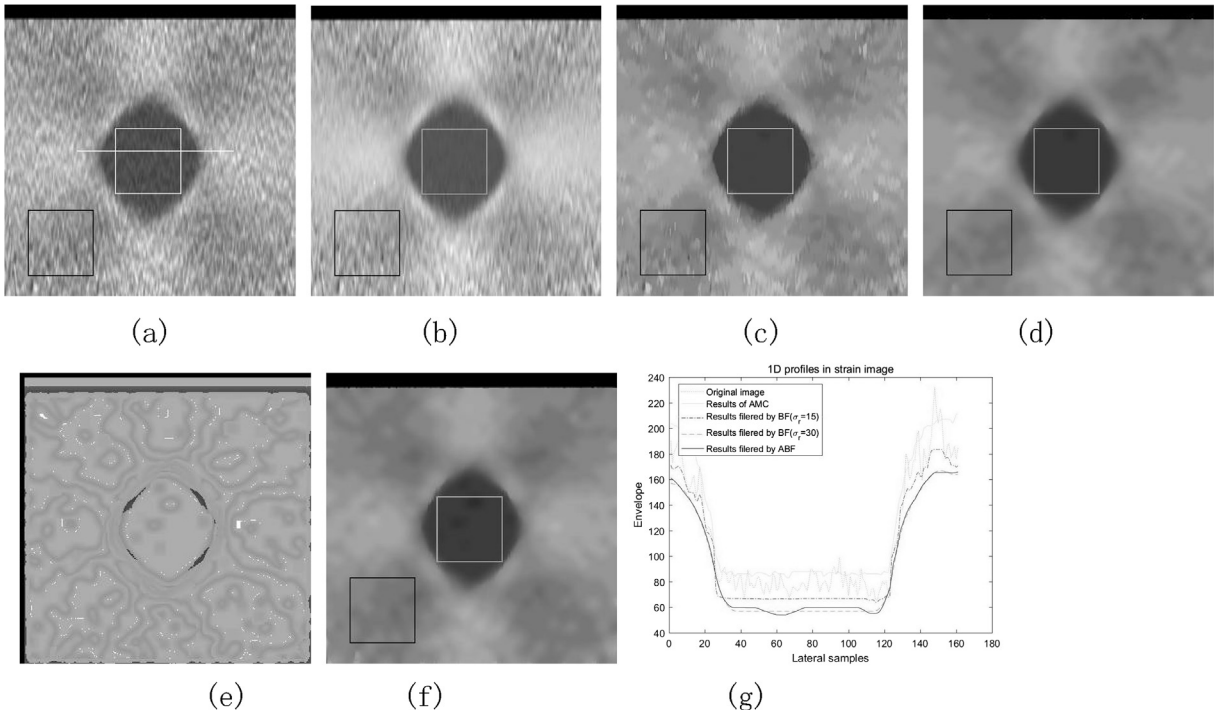

Fig. 5. The correlation window size is 8. Overlap is 0.60. Window size of filter is 11 × 11 pixels. (a) Simulation strain (SNRe = 8.102, CNRe = 26.39); (b) strain after AMC (SNRe = 9.60, CNRe = 39.96); (c) strain after FBF (σr = 15, SNRe = 12.35, CNRe = 75.88); (d) strain after FBF (σr = 30, SNRe = 16.30, CNRe = 153.87) (e) Histogram matching; (f) strain after AFBF (SNRe = 18.63, CNRe = 164.02);(g) 1D profiles in strain image.

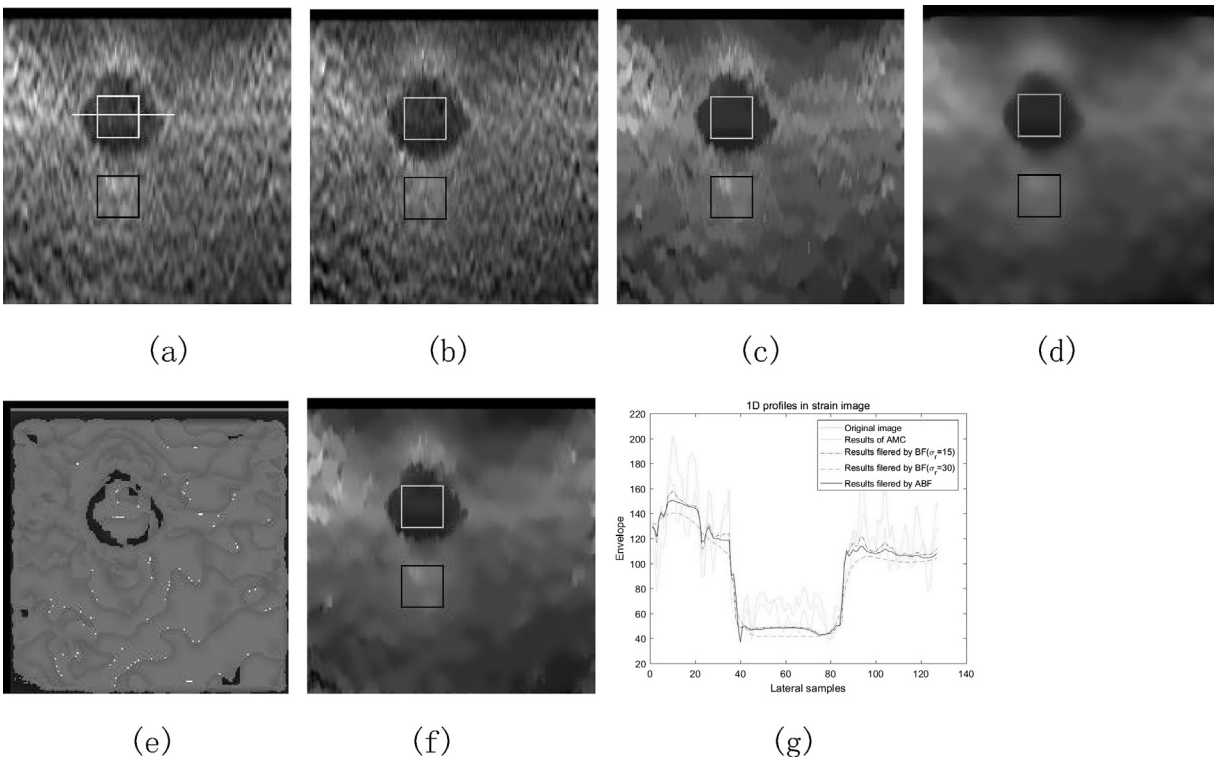

Fig. 6. The correlation window size is 20. Overlap is 0.8. Window size of filter is 11 × 11 pixels. (a) Phantom strain (SNRe = 6.67, CNRe = 18.01); (b) strain after AMC (SNRe = 7.95, CNRe = 23.77); (c) strain after FBF (σr = 15, SNRe = 8.64, CNRe = 42.64); (d) strain after FBF (σr = 30, SNRe = 12.82, CNRe = 83.82) (e) Histogram matching; (f) strain after AFBF (SNRe = 10.17, CNRe = 57.27);(g) 1D profiles in strain image.

is efficient to reduce the artifact noise and, at the same time, maintain the tissue structure. For clear illustration, the profiles, along the highlight line in the original image, are also compared. As indicated by the profiles in Figs. 5(g) and 6(g), our algorithm produces a better result for the purpose of visualization.

6. Conclusion

In this paper we have developed a novel approach of artifacts noise reduction based on an adaptive fast bilateral filtering. The probability distribution function (PDF) of AM noise in this paper is derived from the statistics of uncompressed speckle. The statistical model of artifact formation is useful for designing an adaptive fast bilateral filter for artifacts reduction. Testing in simulation and phantom imaging demonstrates that our method can reduce artifacts noise and preserve the structure at the same time. The proposed technique would have potential applications in clinical freehand ultrasound strain imaging for artifacts noise reduction. However, this paper only gives a preliminary study on the probability distribution function of artifacts noise and artifacts detection of strain imaging. Further works include parameters optimization, the processing in GPU platforms and more in-vivo testing.

Acknowledgment

This work was supported by the Postdoctoral Science Foundation of China (2016M592894XB), the Nature and Science Foundation of China (61741112) and the Nature and Science Foundation of Yunnan Province (2017FB098). We also appreciated the valuable comments from the other members of our department.

Appendix A

The distribution of W

Own to a minute target compression, there is a high degree of correlation between X_1 and X_2 in Eq. (4); we can convert the Eq. (3) into the Eq. (A1).

$$W \approx X_1^2 \approx X_2^2 \approx X^2 \tag{A1}$$

According to [16], the signal envelope amplitude can be considered as an independent random variable. Distribution function of W is as follows.

$$\begin{aligned} F_W(w) &= P\{W \leqslant w\} = P\{X^2 \leqslant w\} \\ &= P\{0 \leqslant X \leqslant w^{1/2}\} \equiv F_X(w^{1/2}) \end{aligned} \tag{A2}$$

According to Eq. (4) and the theory of statistics, the PDF of W is as follows.

$$\begin{aligned} p_W(w) &= [F_W(w)]' = [F_X(w^{1/2})]' = (w^{1/2})' \cdot f_X(w^{1/2}) \\ &= \frac{1}{2\sqrt{w}} \frac{\sqrt{w}}{\sigma_0^2} e^{-\frac{w}{2\sigma_0^2}} = \frac{1}{2\sigma_0^2} e^{-\frac{w}{2\sigma_0^2}} = \lambda e^{-\lambda w} \end{aligned} \tag{A3}$$

where $\lambda = 1/(2{\sigma_0}^2)$. Obviously, W follows exponential distribution.

Appendix B

The PDF of l_m

For the sake of clarity, we convert Eq. (2) into the followings.

$$l_m = \frac{\sum_{t=m\Delta t}^{m\Delta t+n} Y_2}{Y_1} = \frac{Y_3}{Y_1} \tag{B1.1}$$

$$Y_1 = \sum_{t=m\Delta t}^{m\Delta t+n} W(t, d_m) \tag{B1.2}$$

$$Y_2 = W(t, d_m) \cdot t \tag{B1.3}$$

$$Y_3 = \sum_{t=m\Delta t}^{m\Delta t+n} Y_2 \tag{B1.4}$$

According to [42], the sum of random variables, which follows exponential distribution with the same parameter, follows a Gamma distribution. So the probability density function of *Y1* is as follows.

$$p_{Y_1}(y_1) = \frac{\lambda^n y_1^{n-1}}{\Gamma(n)} e^{-\lambda y_1} \tag{B2}$$

According to the theory of statistics, distribution function of Y_2 is as follows.

$$F_{Y_2}(y_2) = P\{Y_2 \leqslant y_2\} = P\{t_n W \leqslant y_2\} = P\left\{W \leqslant \frac{y_2}{t_n}\right\} \equiv F_W\left(\frac{y_2}{t_n}\right) \tag{B3.1}$$

Further, the probability density function of Y_2 is as following.

$$p_{Y_2}(y_2) = [F_{Y_2}(y_2)]' = \left[F_W\left(\frac{y_2}{t_n}\right)\right]' = \left(\frac{y_2}{t_n}\right)' \cdot f_W\left(\frac{y_2}{t_n}\right) = \frac{\lambda}{t_n} e^{-\frac{\lambda y_2}{t_n}} = \lambda_n e^{-\lambda_n y_2} \tag{B3.2}$$

where $\lambda_n = \lambda / t_n = \lambda / n$, $t_n = 1, 2, 3, 4, \ldots, n$. According to [56], the probability density function of Y_3, which is sum of exponential distributions with different parameters, is as following.

$$p_{Y_3}(y_3) = \frac{\lambda^n}{\Gamma(n+1)} \sum_{i=1}^{n} \left[\frac{e^{-\lambda_i y_3}}{\prod_{\substack{j=1 \\ i \neq j}}^{n} (\lambda_j - \lambda_i)} \right] \tag{B4}$$

Set Y_1 and Y_3 are considered as independent random variables. According to probability and statistics theory, the probability density function of l_m is as follows.

$$p_{L_m}(l_m) = \frac{\lambda^{2n}}{\Gamma(n)} \sum_{i=1}^{n} \left[\frac{(\lambda_i l_m + \lambda)^{-(n+1)}}{\prod_{\substack{j=1 \\ i \neq j}}^{n} (\lambda_j - \lambda_i)} \right] \tag{B5}$$

Appendix C

The PDF of Δl

Δl is considered hypothetically as an independent random variable. According to probability and statistics theory and Eq. (7), the distribution function of Δl is as following.

$$F_{\Delta L}(\Delta l) = P\{\Delta L \leqslant \Delta l\} = P\{L'_m \leqslant \Delta l\} = P\left\{L_m \leqslant \frac{\Delta l^2}{2} + c\right\} \equiv F_{L_m}\left(\frac{\Delta l^2}{2} + c\right) \tag{C1}$$

Further more, the probability density function of Δl is as following.

$$\begin{aligned} p_{\Delta L}(\Delta l) &= [F_{\Delta L}(\Delta l)]' = \left[F_{L_m}\left(\tfrac{\Delta l^2}{2} + c\right)\right]' = \left(\tfrac{\Delta l^2}{2} + c\right)' \cdot f_{L_m}\left(\tfrac{\Delta l^2}{2} + c\right) \\ &= \Delta l \cdot f_{L_m}\left(\tfrac{\Delta l^2}{2} + c\right) = A \cdot \sum_{i=1}^{n} \frac{i^{2n-1} \Delta l \cdot \left(\frac{\Delta l^2}{2} + c + i\right)^{-(n+1)}}{\prod_{\substack{j=1 \\ j \neq i}}^{n} (i-j)} \end{aligned} \tag{C2}$$

References

[1] A. Thitaikumar, R. Righetti, T.A. Krouskop, J. Ophir, Resolution of axial shear strain elastography, Phys. Med. Biol. 51 (2006) 5245–5257.
[2] R. Righetti, J. Ophir, A. ThitaiKumar, T. Krouskop, Assessing image quality in effective Poisson's ratio elastography and poroelastography – part II, Phys. Med. Biol. 52 (2007) 1321–1333.
[3] Arun Thitaikumar, Louise M. Mobbs, Christina M. Kraemer-Chant, Brian S. Garra, Jonathan Ophir, Breast Tumor Classification using axial shear strain elastography: a feasibility study, Phys. Med. Biol. 53 (2008) 4809–4823.
[4] T.A. Krouskop, T.M. Wheeler, F. Kallel, T. Hall, The elastic moduli of breast and prostate tissues under compression, Ultrason. Imaging 20 (1998) 260–274.
[5] R. Righetti, F. Kallel, R.J. Stafford, R.E. Price, T.A. Krouskop, J.D. Hazle, J. Ophir, Elastographic characterization of HIFU-induced lesions in canine livers, Ultrasound Med. Biol. 25 (7) (1999) 1099–1113.
[6] E.E. Konofagou, J. D'hooge, J. Ophir, Myocardial elastography—A feasibility study, Ultrasound Med. Biol. 28 (4) (2002) 113–132.
[7] T. Varghese, J. Zagzebski, J. Jee, Elastography imaging of thermal lesion in the liver in vivo following radio frequency ablation: preliminary results, Ultrasound Med. Biol. 28 (2002) 1467–1473.
[8] J. Luo, J. Bai, P. He, K. Ying, Axial strain calculation using a low-pass digital differentiator in ultrasound elastography, IEEE Trans. Ultrason. Ferroelectr. Freq. Control vol.51, (no.9) (sep. 2004) 1119–1127.
[9] J. Lindop, G. Treece, A. Gee, R. Prager, The general properties including accuracy and resolution of linear filtering methods for strain estimation, IEEE Trans. Ultrason. Ferroelectr. Freq. Control vol.55, (no.11) (nov. 2008) 2363–2368.
[10] M. O'Donnell, A.R. Skovoroda, B.M. Shapo, S.Y. Emelianov, Internal displacement and strain imaging using ultrasonic speckle tracking, IEEE Trans. Ultrason., Ferroelect., Freq. Contr. 41 (3) (1994) 314–325, https://doi.org/10.1109/58.285465.
[11] A. Pesavento, C. Perrey, M. Krueger, H. Ermert, A time-efficient and accurate strain estimation concept for ultrasonic elastography using iterative phase zero estimation, IEEE Trans. Ultrason. Ferroelectr. Freq. Control vol.46, (no.5) (sep.1999) 1057–1067.
[12] J. Lindop, G. Treece, A. Gee, R. Prager, Phase-based ultrasonic deformation estimation, IEEE Trans. Ultrason. Ferroelectr. Freq. Control 55 (1) (Jan. 2008) 94–111.
[13] J.W. Goodman, Speckle Phenomena in Optics, Roberts&Co, Greenwood Village Co, 2006.
[14] I. Céspedes, J. Ophir, Reduction of image noise in elastography, Ultrason. Imaging 15 (2) (1993) 89–102.
[15] T. Varghese, J. Ophir, I. Cespedes, Noise reduction in elastograms using temporal stretching with multicompression averaging, Ultrasound Med. Biol. 22 (1996) 1043–1052.
[16] S.K. Alam, J. Ophir, E.E. Konofagou, An adaptive strain estimator for elastography, IEEE Trans. Ultrason. Ferroelec. Freq. Control 45 (2) (1998) 461–472.
[17] U. Techavipoo, T. Varghese, Wavelet de-noising of displacement estimates in elastography, Ultrasound Med. Biol. 30 (4) (2004) 477–491.
[18] Joel Lindop, Graham Treece, Andrew Gee, Richard Prager, Estimation of displacement location for enhanced strain imaging, IEEE Trans. Ultrason., Ferroelect., Freq. Contr. 54 (9) (2007) 1751–1771.
[19] U. Techavipoo, Q. Chen, T. Varghese, J.A. Zagzebski, E.L. Madsen, Noise reduction using spatial-angular compounding for elastography, IEEE Trans. Ultrason. Ferroelec. Freq. Control 51 (5) (2004) 510–520.
[20] Q. Chen, A. Gerig, U. Techavipoo, J.A. Zagzebski, T. Varghese, Correlation of RF signals during angular compounding, IEEE Trans. Ultrason. Ferroelectr. Freq. Control 52 (6) (Jun. 2005) 961–970.
[21] H.H.G. Hansen, R.G.P. Lopata, C.L. De Korte, Noninvasive carotid strain imaging using angular compounding at large beam steered angles: validation in vessel phantoms, IEEE Trans. Med. Imaging 28 (6) (2009) 872–880.
[22] Kun Zhang, Paul Liu, Dong C. Liu, Strain image with spatial angular compounding, International Conference on Bioinformatics and Biomedical Enginerring (ICBBE 2010), (2010).
[23] Wen Liu, Yangjie Cheng, Paul Liu, Dong C. Liu, Filter Based Spatial Compounding for Strain Imaging, Proceedings of 2010 IEEE 17th International Conference on Image Processing September 26-29, 2010, Hong Kong, (2010).
[24] Paul Liu, Dong Liu, Filter-based compounded delay estimation with application to strain imaging, vol 58, IEEE Trans. Ultrason. Ferroelec. Freq. Control 58 (10) (2011) 2078–2095.
[25] Yangjie Cheng, Shaoguo Cui, Paul Liu, Dong C. Liu, Frequency compounding for ultrasound freehand elastography, The 4rd International Conference on Bioinformatics and Biomedical Engineering (ICBBE 2010), (2010).
[26] Shaoguo Cui, Dong C. Liu, Noise reduction for ultrasonic elastography using transmit-side frequency compounding: a preliminary study, IEEE Trans. Ultrason. Ferroelec. Freq. Control 58 (2011) no.3.
[27] X. Zhou, W. Liu, C. Zhang, D.C. Liu, Speckle reduction of ultrasound elastography with bilateral filter, Adv. Sci. Lett. 11 (4) (2013) 3025–3027.
[28] Mohammad Arafat Hussain, Farzana Alam, Sharmin Akhtar Rupa, Rayhana Awwal, Md Kamrul Hasan, Lesion edge preserved direct average strain estimation for ultrasound elasticity imaging, Ultrasonics 54 (1) (2014) 137–146.
[29] Dangguo Shao, Ming Zhong, Dong C. Liu, A fast bilateral filter with application to artifact reduction, Comp. Meth. Biomech. Biomed. Eng. 18 (4) (2015) 376–381.
[30] Renaud Morin, Adrian Basarab, Stéphanie Bidon, Denis Kouamé, Motion estimation-based image enhancement in ultrasound imaging, Ultrasonics 60 (July 2015) 19–26.
[31] Wenxia Wang, Hu. Danfeng, Jiajun Wang, Wei Zou, Strain estimation by a Fourier Series-based extrema tracking algorithm for elastography, Ultrasonics 62 (September 2015) 278–291.

[32] Rifat Ahmed, Rishad Arfin, Monir Hossan Rubel, Kazi Khairul Islam, S. Kaisar Alam, Comparison of windowing effects on elastography images: simulation, phantom and in vivo studies, Ultrasonics 66 (March 2016) 140–153.
[33] Md. Shifat-E Rabbi, Md. Kamrul Hasan, Speckle tracking and speckle content based composite strain imaging for solid and fluid filled lesions, Ultrasonics 74 (2017) 124–139.
[34] S.K. Alam, J. Ophir, T. Varghese, Elastographic axial resolution criteria: an experimental study, IEEE Trans. Ultrason., Ferroelectrics, Freq. Control 47 (1) (January 2000) 304–309.
[35] Raffaella Righetti, Seshadri Srinivasan, Jonathan Ophir, Lateral resolution in elastography, Ultrasound Med. Biol. 29 (5) (2003) 695–704.
[36] Dong C. Liu, S. Czenszak, J. Kim, Adaptive strain noise reduction with color transparency display, Proc. of IEEE Ultrason. Symp. (1998) 1611–1614.
[37] X.Y. Li, D.C. Liu, Ultrasound strain noise reduction based on image segmentation and diffused region growing, 9th International Conference on Computer Vision, Pattern Recognition and Image Processing, (2008).
[38] M. Elad, On the origin of the bilateral filter and ways to improve it, IEEE Trans. Image Process. 11 (10) (2002) 1141–1151.
[39] S. Bae, S. Paris, F. Durand, Two-scale tone management for photographic look, ACM Trans. Graph. 25 (3) (2006) 637–645.
[40] Simon Perreault, Patrick He′bert, Median filtering in constant time, Image Process., IEEE Trans. on 16 (2007) 2389–2394.
[41] Huang Lingyun, Petrank Yael, Huang Sheng-Wen, Jia Congxian, O'Donnell Matthew, Phase rotation methods in filtering correlation coefficients for ultrasound speckle tracking, IEEE Trans. Ultrason., Ferroelectrics, Freq. Control Vol. 56 (No.7) (2009).
[42] Mohamed Akkouchi, On the convolution of exponential distributions, J. Chungcheong Math. Soc. 21 (4) (December 2008).